Automated Motion Correction for *In Vivo* Optical Projection Tomography

Shouping Zhu, Di Dong, Udo Jochen Birk, Matthias Rieckher, Nektarios Tavernarakis, Xiaochao Qu, *Member, IEEE*, Jimin Liang, *Member, IEEE*, Jie Tian, *Fellow, IEEE*, and Jorge Ripoll*

***Abstract*—In *in vivo* optical projection tomography (OPT), object motion will significantly reduce the quality and resolution of the reconstructed image. Based on the well-known Helgason–Ludwig consistency condition (HLCC), we propose a novel method for motion correction in OPT under parallel beam illumination. The method estimates object motion from projection data directly and does not require any other additional information, which results in a straightforward implementation. We decompose object movement into translation and rotation, and discuss how to correct for both translation and general motion simultaneously. Since finding the center of rotation accurately is critical in OPT, we also point out that the system's geometrical offset can be considered as object translation and therefore also calibrated through the translation estimation method. In order to verify the algorithm effectiveness, both simulated and *in vivo* OPT experiments are performed. Our results demonstrate that the proposed approach is capable of decreasing movement artifacts significantly thus providing high quality reconstructed images in the presence of object motion.**

***Index Terms*—Helgason–Ludwig consistency condition (HLCC), motion correction, optical projection tomography (OPT).**

I. Introduction

OPTICAL projection tomography (OPT) has emerged as a powerful tool for 3-D reconstruction of specimens with dimensions of 1–10 mm across [1]–[3]. It is the optical equivalent of X-ray computed tomography (CT), and thus is also known as optical CT [4]–[7]. In the past few years, OPT has been widely used for imaging small biological samples with high resolution and sensitivity, such as murine embryos, zebra fish embryos, nematode *Caenorhabditis elegans*, *Drosophila melanogaster*, small animal organs, and plant sections [6]–[12]. Additionally, several groups have focused their research on OPT in order to improve its resolution, reduce artifacts and noise, and expand its application to live imaging and 4-D imaging [13]–[26]. OPT is most commonly used with parallel beam illumination, in which case the theoretical basis for OPT reconstruction is the inverse Radon transform. This requires the assumption that the specimen remains stationary during the entire scan. However, the assumption is not always satisfied, especially in *in vivo* OPT applications [27], [28]. Specimen movement will introduce artifacts in the reconstructed image and degrade spatial resolution considerably. Thus, it is necessary to implement motion correction in *in vivo* OPT, and the main reason that microscopic OPT is capable of delivering high resolution images is the capability for motion error correction which becomes increasingly important and imperative at microscopic scales. In a previous paper, we presented a set of correction methods applied to calibrate object motion [29]. Tracking markers from fluorescent data were utilized to determine object motion. Since the methodology employed was not automated in this previous work, we now focus our attention on the development of automated methods. The objective of the current work is therefore to study the more general case of marker-free methods to estimate object motion automatically.

With regards to motion artifacts, a similar situation also appears in fan beam and cone beam X-ray CT imaging, where motion calibration methods have been widely studied [30]–[33]. The well-known Helgason–Ludwig consistency condition (HLCC) is a mathematical constraint on projection data and reveals the redundancy of projection data [34]. It has been utilized to reduce X-ray CT image artifacts and to estimate unknown view angles [35], [36]. Based on this consistency condition, Yu *et al.* proposed motion estimation methods for fan-beam X-ray CT scanner [37], [38]. Using an equivalent approach, we make use of the consistency condition to account for specimen motion in parallel beam OPT.

In this paper, we describe an estimation method to calibrate the motion of the specimen in parallel beam OPT. We demonstrate the efficiency of the method both by simulated and *in vivo* OPT experiments, in which we image the model organism *Caenorhabditis elegans*. The paper is organized as follows. In Section II, we describe our estimation method for parallel beam OPT motion, and in Section III, we demonstrate the accuracy of the method through both simulated and *in vivo* OPT data. In

Manuscript received January 19, 2012; accepted February 13, 2012. Date of publication February 24, 2012; date of current version June 26, 2012. This work was supported in part by the Bill and Melinda Gates Foundation, in part by the National Basic Research Program of China (973 Program) under Grant 2011CB707702, in part by the the National Natural Science Foundation of China under Grant 81090272 and Grant 81101084, in part by the Fellowship for Young International Scientists of the Chinese Academy of Sciences under Grant 2010Y2GA03, and in part by the Fundamental Research Funds for the Central Universities. *Asterisk indicates corresponding author.*

S. Zhu, X. Qu, and J. Liang are with the School of Life Sciences and Technology, Xidian University, Xi'an, Shaanxi 710071, China.

D. Dong is with the Intelligent Medical Research Center, Institute of Automation, Chinese Academy of Sciences, Beijing 100190, China.

M. Rieckher and N. Tavernarakis are with the Institute of Molecular Biology and Biotechnology, Foundation for Research and Technology-Hellas (FORTH), 71110 Heraklion, Greece.

U. J. Birk is with the Institute of Electronic Structure and Laser, Foundation for Research and Technology-Hellas (FORTH), 71110 Heraklion, Greece and also with the University of Heidelberg, Kirchhoff Institute for Physics, INF 227, 69120 Heidelberg, Germany.

J. Tian is with the School of Life Sciences and Technology, Xidian University, Xi'an, Shaanxi 710071, China and also with the Intelligent Medical Research Center, Institute of Automation, Chinese Academy of Sciences, Beijing 100190, China.

*J. Ripoll is with the Institute of Electronic Structure and Laser, Foundation for Research and Technology-Hellas (FORTH), 71110 Heraklion, Greece. (e-mail: jripoll@iesl.forth.gr).

Digital Object Identifier 10.1109/TMI.2012.2188836

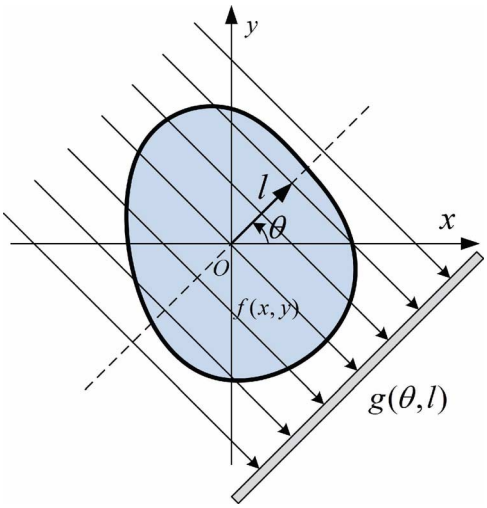

Fig. 1. Geometry of parallel beam projection.

Section IV, we present the results, finally including discussion and conclusions in Section V.

II. Methods

A. Parallel Beam Consistency Conditions

Considering the case of OPT with parallel beam illumination, as shown in Fig. 1, let $f(x,y)$ be a slice to be reconstructed, which represents the density distribution of the light absorption map of the sample. Let $g(\theta,l)$ be the line integral of $f(x,y)$ along a certain line at a distance l from the origin and at an angle θ with the x-axis. The relationship between $f(x,y)$ and $g(\theta,l)$ can be defined by the well-known Radon transform as

$$g(\theta,l)=\iint_C f(x,y)\delta(x\cos\theta+y\sin\theta-l)\,\mathrm{d}x\,\mathrm{d}y \tag{1}$$

where $\delta(\cdot)$ represents the Dirac delta function.

The relationship between $g(\theta,l)$ and $f(x,y)$ can also be described by their geometry and k-order moments. The geometry moment of $f(x,y)$ is expressed as

$$m_{i,j}=\iint_C x^i y^j f(x,y)\,\mathrm{d}x\,\mathrm{d}y \tag{2}$$

where i and j are nonnegative integers. The k-order moment of $g(\theta,l)$ is

$$v_k(\theta)=\int_{-\infty}^{+\infty} l^k g(\theta,l)\,\mathrm{d}l \tag{3}$$

where k is a nonnegative integer. Then the relationship between (2) and (3) can be expressed by the Helgason Ludwig consistency condition as follows:

$$v_k(\theta)=\sum_{r=0}^{k}\frac{k!}{r!(k-r)!}m_{r,k-r}\cos^r\theta\sin^{k-r}\theta. \tag{4}$$

The HLCC is important for parallel-beam CT, and is the theoretical basis on which we will work on to estimate the motion parameters in OPT. The consistency condition can be found in [34], and a full derivation of (4) is given in Appendix A.

B. Rigid Motion in Parallel Beam Geometry

In this paper, object motion in parallel beam OPT is assumed to be rigid motion which decomposes into translation $(d_x(t),d_y(t))$ and rotation $\phi(t)$ components, where $0\le t\le T$ with T representing the virtual total scanning time. The unit of T is in seconds. Denoting T as virtual total scanning time indicates that T differs from the actual total scanning time T_0 in an OPT experiment. The relationship between T and T_0 can be expressed as $T=\alpha T_0$, where α is a positive scale coefficient. There are two reasons to introduce the virtual total scanning time T. First, in many cases the accurate actual total scanning time T_0 is unknown when processing the OPT data, unless an accurate time-stamp is saved with each image. Second and most important, a suitable choice of T is of benefit to improve the robustness of the motion estimation algorithm, which will be shown in this subsection. At the same time, using a virtual total scanning time T to replace T_0 will not affect the motion estimation results, proof of which will be shown in Appendix B.

At a certain time t, the scanning angle is represented by $\theta(t)=\omega t+\phi(t)$, where $\omega=2\pi/T$ is the rotation angle frequency. It should be stated that in this work we have only considered rotation of the specimen along the axis of the OPT rotation, which is usually the only allowed rotation axis since typical specimens are constrained during the imaging process (in the examples shown here the nematode is placed inside a thin capillary, for example). One of the main effects of sample rotation along the OPT axis is that the data will not have evenly distributed projections, and possibly not even cover the full 360°. If this is not accounted for and calibrated, it will significantly degrade the quality of the filtered backprojection (FBP) method.

Let us now assume that there is a point $P(x,y)$ in the object, which in the absence of motion should be projected to position l at angle θ. Due to object motion it will now be projected to a new position $\bar{l}$ as

$$\bar{l}=l-d_x(t)\cos(\theta(t))-d_y(t)\sin(\theta(t)). \tag{5}$$

By replacing l in (3) by $\bar{l}$, we obtain

$$\begin{aligned}v_k(\theta)&=\int_{-\infty}^{+\infty}\bar{l}^k f(x,y)\,\mathrm{d}\bar{l}\\&=\int_{-\infty}^{+\infty}[l-d_x(t)\cos(\theta(t))-d_y(t)\sin(\theta(t))]^k\\&\quad\times g(\theta,l)\,\mathrm{d}l.\end{aligned} \tag{6}$$

Through substitution of (6) into (4) we get the consistency condition for object motion

$$\begin{aligned}v_k(\theta)&=\int_{-\infty}^{+\infty}[l-d_x(t)\cos(\theta(t))-d_y(t)\sin(\theta(t))]^k g(\theta,l)\,\mathrm{d}l\\&=\sum_{r=0}^{k}\frac{k!}{r!(k-r)!}m_{r,k-r}\cos^r(\theta(t))\sin^{k-r}(\theta(t)).\end{aligned} \tag{7}$$

For each k there will be an independent equation to describe the relationship between the projection data $g(\theta,l)$ and the object function $f(x,y)$.

C. Translational Motion Estimation

First of all, let us assume that there exists translation motion only, namely $\phi(t) = 0$. In order to estimate translation motion through the HLCC, let $k = 1$ in (7) in which case we have

$$C_1(t) - C_0(t)d_x(t)\cos(\theta(t)) - C_0(t)d_y(t)\sin(\theta(t)) = m_{0,1}\sin(\theta(t)) + m_{1,0}\cos(\theta(t)) \quad (8)$$

where $C_0(t) = \int_{-\infty}^{+\infty} g(\theta(t), l)\ \mathrm{d}l$, and $C_1(t) = \int_{-\infty}^{+\infty} l g(\theta(t), l)\,\mathrm{d}l$. In fact, if we consider $f(x, y)$ as a density function of an object, then $C_0(t)$ is the total mass of the object and is thus independent of the virtual scanning time t, in which case we denote $C_0(t)$ as C_0. Since C_0 represents the sum of the light attenuation coefficient of the sample, we may safely assume that C_0 is a positive value throughout the sample and will equal zero only when there is no sample, in which case sample motion is not relevant. Dividing both sides of the above equation by C_0 yields

$$\frac{C_1(t)}{C_0} = \left(\frac{m_{1,0}}{C_0} + d_x(t)\right)\cos(\theta(t)) + \left(\frac{m_{0,1}}{C_0} + d_y(t)\right)\sin(\theta(t)). \quad (9)$$

Now let us consider that $d_x(t)$ and $d_y(t)$ are smooth and continuous, which is a suitable assumption to describe motion in OPT. In this case we can approximate $d_x(t)$ and $d_y(t)$ to an N_1-order polynomial as

$$\begin{cases} d_x(t) = p_{1,0} + p_{1,1}t + \cdots + p_{1,N_1}t^{N_1} \\ d_y(t) = p_{2,0} + p_{2,1}t + \cdots + p_{2,N_1}t^{N_1}. \end{cases} \quad (10)$$

It should be noted that in (10) we express the motion through a polynomial function for simplicity. In fact, decomposition into Bessel or Fourier components can also be used to approximate $d_x(t)$ and $d_y(t)$ [37]. Considering $d_x(0) = 0$ and $d_y(0) = 0$, we have $p_{1,0} = p_{2,0} = 0$, then

$$\begin{cases} d_x(t) = p_{1,1}t + \cdots + p_{1,N_1}t^{N_1} \\ d_y(t) = p_{2,1}t + \cdots + p_{2,N_1}t^{N_1}. \end{cases} \quad (11)$$

Assuming the OPT setup works in a rotate and shoot mode, we may denote $0 = t_0 < t_1 < \cdots < t_J = T$ as the scanning time, and acquire $J + 1$ projections over the 360° coverage. Substituting (11) into (9), and letting $\bar{m}_{0,1} = m_{0,1}/C_0$ and $\bar{m}_{1,0} = m_{1,0}/C_0$, we will have the following system equation in matrix form

$$\mathbf{Q} = \mathbf{MP} \quad (12)$$

where

$$\mathbf{Q} = \left[\frac{C_1(t_0)}{C_0}, \frac{C_1(t_1)}{C_0}, \ldots, \frac{C_1(t_J)}{C_0}\right]^T \quad (13)$$

$$\mathbf{P} = [\bar{m}_{0,1}, p_{1,1}, p_{1,2}, \ldots, p_{1,N_1}, \bar{m}_{1,0}, p_{2,1}, p_{2,2}, \ldots, p_{2,N_1}]^T. \quad (14)$$

In the above equations, $\mathbf{Q}$ is calculated from projection data, while $\mathbf{P}$ is the vector to be estimated. It is easy to prove that each row of $\mathbf{M}$ is independent. If the number of projections is larger than the number of coefficients which need to be determined, i.e., $(J+1) > 2(N_1+1)$, a condition which is satisfied in most practical cases, (12) will be an overdetermined equation. In this case we can solve it through a least mean squares or a singular value decomposition method.

D. Condition Number Analysis

It is well known that the condition number of matrix $\mathbf{M}$ will significantly affect numerical stability in solving (12), so we will dedicate this subsection to the condition number of $\mathbf{M}$. Denote the condition number of matrix $\mathbf{M}$ by $\mathrm{Cond}(\mathbf{M}) = \sigma_1/\sigma_q$, where σ_1 and σ_q are the maximum and minimum singular values of matrix $\mathbf{M}$, respectively, and where $q = 2(N_1 + 1)$.

From (15), shown at the bottom of the page, we can see that $\mathbf{M}$ is a function of t_j, where $j = 0, \ldots, J$. Assuming that we perform equal angle step scanning in OPT imaging, then $t_j = j\Delta T$, where $\Delta T = T/J$. Therefore, the choice of T will affect the condition number of matrix M. In order to show the effect of T on the matrix $\mathbf{M}$ condition number, we plot the $\mathrm{Cond}(\mathbf{M})$ with T in Fig. 2 for the case $J = 359$ and $N_1 = 3$. From this figure we can see that the value of T affects the $\mathbf{M}$ condition number significantly, as expected. $\mathrm{Cond}(\mathbf{M})$ reaches its minimum value at $T = 1.40$ s and increases greatly when T grows or shrinks. It indicates that the suitable T should be chosen during translation estimation to enhance algorithm stability. It should be pointed out again that the choice of the virtual total scanning time T is not limited by the actual total scanning time T_0 as we have mentioned above. We will give a detailed proof in Appendix B.

In Table I, we list the minimum $\mathrm{Cond}(\mathbf{M})$ value and corresponding T for different order polynomials N_1, with $J = 359$. It is found that we have to choose the value for N_1 carefully, since $\mathrm{Cond}(\mathbf{M})$ will quickly increase with N_1, while at the same time an accurate description of the object's movement requires the largest possible N_1. In addition, during our study we find that $\mathrm{Cond}(\mathbf{M})$ is insensitive to J as long as $(J+1) > 2(N_1+1)$ due to the independence of each row of matrix $\mathbf{M}$.

$$\mathbf{M} = \begin{bmatrix} \cos\theta(t_0), & t_0\cos\theta(t_0), & \ldots, & t_0^{N_1}\cos\theta(t_0), & \sin\theta(t_0), & t_0\sin\theta(t_0), & \ldots, & t_0^{N_1}\sin\theta(t_0) \\ \cos\theta(t_1), & t_1\cos\theta(t_1), & \ldots, & t_1^{N_1}\cos\theta(t_1), & \sin\theta(t_1), & t_1\sin\theta(t_1), & \ldots, & t_1^{N_1}\sin\theta(t_1) \\ \vdots & \vdots & \ddots & \vdots & \vdots & \vdots & \ddots & \vdots \\ \cos\theta(t_J), & t_J\cos\theta(t_J), & \ldots, & t_J^{N_1}\cos\theta(t_J), & \sin\theta(t_J), & t_J\sin\theta(t_J), & \ldots, & t_J^{N_1}\sin\theta(t_J) \end{bmatrix} \quad (15)$$

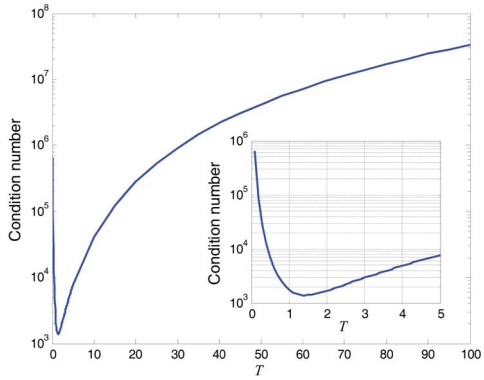

Fig. 2. Behavior of the Condition Number of $\mathbf{M}$ with respect to the virtual total scanning time T.

TABLE I
MINIMUM $\mathrm{Cond}(\mathbf{M})$ AND CORRESPONDING VIRTUAL TOTAL SCANNING TIME (T) VALUES FOR DIFFERENT ORDER POLYNOMIALS N_1

N_1	1	2	3	4
$\min\{\mathrm{Cond}(\mathbf{M})\}$	4.60	54.11	1384.90	52595.24
T	1.61	1.55	1.40	1.30

E. Physical Meaning of the Translation Estimation Method

Once we have defined the equations which may account for object movement, we shall now resort to explaining the physical meaning of these equations. By defining $\bar{d}_x(t) = \bar{m}_{1,0} + d_x(t)$ and $\bar{d}_y(t) = \bar{m}_{0,1} + d_y(t)$, (9) becomes

$$\frac{C_1(t)}{C_0} = \bar{d}_x(t)\cos(\theta(t)) + \bar{d}_y(t)\sin(\theta(t)). \tag{16}$$

As mentioned above, C_0 is related to the total density of the object and hence is equivalent to its total mass. In this case, $C_1(t)/C_0$ denotes the mass center of the projection at time t, the point $(\bar{m}_{1,0}, \bar{m}_{0,1})$ representing the mass center of the object, $f(x, y)$, at time $t = 0$. Considering the motion of the object to be described by $d_x(t)$ and $d_y(t)$, in this case the mass center of $f(x, y)$ will be located at $(\bar{d}_x(t), \bar{d}_y(t))$ at time t. That is to say, $(\bar{d}_x(t), \bar{d}_y(t))$ represents the motion trajectory of the object. In light of the above, the meaning of (16) is now clear: it builds a relationship between the mass center of the object and the mass center of its projection, as schematically represented in Fig. 3. If there is no object motion, the projection of the object's center of mass on the detector will form a perfect sinogram. In the case where some movement of the object exists, the perfect sinogram will be altered: this deviation from the perfect sinogram contains the motion information of the object.

F. Calibration of Axis of Rotation Offset

Accurate determination of the axis of rotation is crucial for high resolution OPT. In an ideal case, the projection of the rotation axis will fall on the central row of the detector plane in a parallel beam OPT system. If there is an offset value Δl from the true axis of rotation during scanning and it is not accounted for during reconstruction, the resulting reconstruction will be correspondingly blurred. By using the translation equations presented in the previous subsections, we may convert this geometry offset into an object translation which can be then estimated through the HLCC-based translation estimation method. This means that the presented method is able to estimate not only the object translation motion, but also the offset from the true axis of rotation *simultaneously*.

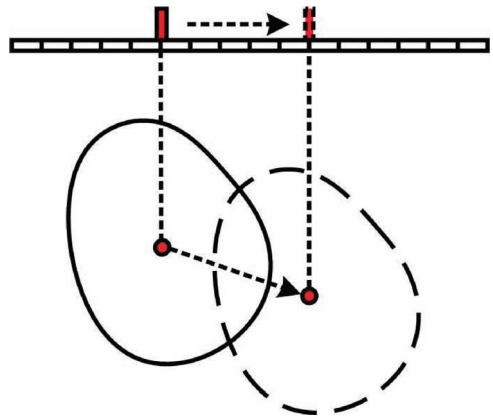

Fig. 3. Physical Meaning of the translation estimation method. Assuming a rigid object, its translation can be considered as the translation of its mass center. Accordingly, the mass center of the projection data will move on the detector plane following the translation of the object's mass center.

G. General Motion Estimation

In all the above description we so far neglected the object rotation. We shall now discuss the case when both translation and rotation motion take place simultaneously, in which case the complexity of the problem clearly increases due to the coupling between the unknown parameters of translation and rotation. Due to this reason, it is impossible to estimate both translation and rotation parameters through the first-order HLCC, and we need to resort to the second-order HLCC to estimate the general motion, which now includes both translation and rotation.

Let $k = 2$ in (4), we have

$$v_2(\theta) = m_{0,2}\sin^2(\theta) + 2m_{1,1}\cos(\theta)\sin(\theta) + m_{2,0}\cos^2(\theta) \tag{17}$$

where $\theta = \theta(t) = \omega t + \phi(t)$. Similarly to the translation case, we approximate $\phi(t)$ by a finite order polynomial as

$$\phi(t) = p_{31}t + p_{32}t^2 + \cdots + p_{3N_2}t^{N_2}. \tag{18}$$

During our motion estimation, the data we can use are the projection data of each angle. So $v_2(\theta(t))$ should be calculated by the following equation which is derived from (6):

$$v_2(\theta) = \int_{-\infty}^{+\infty} [l - d_x(t)\cos(\theta) - d_y(t)\sin(\theta)]^2 g(\theta, l)\, \mathrm{d}l. \tag{19}$$

It is easy to prove that $v_2(\theta(t)) = v_2(\theta(t) + \pi)$ through the symmetry of the cosine and sine functions in (17). Thus, we can construct the following cost function:

$$E = \sum_{j\in\Xi}(v_2(\theta(t_j)) - v_2(\theta(t_j) + \pi))^2 \tag{20}$$

where $\Xi = \{j \mid \theta(t_j) \in [0, \pi]$ and $(\theta(t_j) + \pi) < \max\{\theta(t)\}\}$. It should be noted that the $v_2(\theta(t_j))$ value in the above equation is

calculated through (19), and the $v_2(\theta(t_j)+\pi)$ value is calculated through linear interpolation of $v_2(\theta(t_m))$ and $v_2(\theta(t_n))$, being $\theta(t_m)$ and $\theta(t_n)$ such that $\theta(t_m) < \theta(t_j) + \pi < \theta(t_n)$. Because of the existence of the specimen translation and rotation, the above $v_2(\theta(t_j))$ and $v_2(\theta(t_j)+\pi)$ will cancel out only when the motion values are compensated accurately in (19). That is to say, when the estimated translation and rotation values are equal to the actual motion values, the cost function E will reach its minimum value. Since the translation and rotation parameters are coupled together, a search strategy is used to estimate translation and rotation alternatively. Herein, we give an example of the general motion estimation pseudo-code for $N_2 = 2$.

1) Given search range $[\mathrm{R_{1s}}, \mathrm{R_{1d}}]$ and search step $\Delta \mathrm{R}_1$ for p_{31}, and $[\mathrm{R_{2s}}, \mathrm{R_{2d}}]$ and step $\Delta \mathrm{R}_2$ for p_{32}.
2) For $p_{31} = \mathrm{R_{1s}}$ to $\mathrm{R_{1d}}$ with step $\Delta \mathrm{R}_1$.
3) For $p_{32} = \mathrm{R_{2s}}$ to $\mathrm{R_{2d}}$ with step $\Delta \mathrm{R}_2$.
4) Calculate $\phi(t)$ by (18), and $\theta(t) = \omega t + \phi(t)$.
5) Estimate translation $d_x(t)$ and $d_y(t)$ by (12).
6) Calculate the cost function E for each pair p_{31} and p_{32}.
7) End For p_{32}.
8) End for p_{31}.
9) Find p_{31} and p_{32} for the minimum cost function E.
10) Determine $d_x(t)$ and $d_y(t)$ by (12) for the above p_{31} and p_{32}.

In line 1, the search range and step are input values. In lines 2 to 8, we search the best p_{31} and p_{32} in 2-D space. It is clear that if we express $\phi(t)$ by a three-order polynomial function, we have to perform a 3-D search which will increase the computation burden significantly. An effective method to decrease computation time is to specify a large search range and large step as a first attempt to coarsely determine p_{31} and p_{32}, and then decrease the search range and perform a finer search in the small search space, in order to obtain a more accurate p_{31} and p_{32}. The determination of the search ranges of p_{31} and p_{32} is crucial for motion estimation. In most cases of OPT scanning, the rotation value $\phi(t)$ should not be very large, 30° at most for example. We can initialize both $[R_{1s}, R_{1d}]$ and $[R_{2s}, R_{2d}]$ to $[-30, +30]$, and then perform the above optimization with a large step. If there exists a local minimum of E in the search space, we will decrease the search range and perform a finer search in the small search space. If the local minimum falls on the edge of the search space, we will reset the search range in order to place the minimum found in the center of the search space and perform the optimization once again. In the results presented in this work we made use of the force-search method for the motion estimation, but of course other methods can be used to reach the global optimum solution [39].

III. Experiments

To demonstrate our algorithms for motion correction, we performed two sets of experiments: the first set of experiments was designed in such a way as to correct translation motion, axis of rotation or geometry offset and rotation motion with simulated data. The second set aimed at understanding how the proposed algorithm could be applied to parallel beam OPT imaging. For all of the experiments we set $N_1 = 3$ for translation estimation and $N_2 = 2$ for rotation estimation.

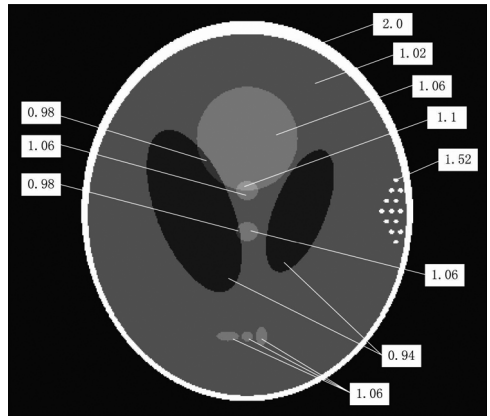

Fig. 4. Modified Shepp–Logan phantom.

TABLE II
Translation and Rotation Function in Numerical Simulations

motion type	function
Translation 1	$d_x(t) = -1.2t + 9t^2$, $d_y(t) = (5.0t - 4.5t^2)$
Translation 2	$d_x(t) = 5\sin(0.75\pi t)$, $d_y(t) = -4(1 - \cos(0.5\pi t)$
Rotation	$\phi(t) = 0.4t - 8.6t^2$

A. Numerical Simulations

In order to demonstrate the feasibility of the proposed algorithm, we performed numerical tests using a modified Shepp–Logan head phantom. Some high contrast points of small size were added to the phantom to further enhance the motion effect, as shown in Fig. 4.

During the experiments, simulated projection data were generated through an analytical line integral, adding 0.1% Gaussian noise so as to verify the robustness of our methods. We supposed that there were 512 detector cells on an equal-spaced detector and 360 projection images were acquired over the full-scan of 360°, i.e., one for every degree. For image reconstruction we made use of a classical FBP method with a Ram–Lak filter [40] where each reconstructed image consisted of 512×512 pixels. It should be noted that since all the simulations were performed in a parallel beam geometry as pertains to current OPT setups, we simply set the pixel size as detector cell size without the need to give the physical dimensions of the pixels. Due to this fact, translation motion is described in pixels in the following experiments.

1) Translation Simulation: Two types of translation motions were simulated in our experiments as shown in Table II, and the corresponding experiments 1 and 2, are listed in Table III. Translation 1 simulated a polynomial curve, while translation 2 simulated a sinusoidal curve motion. The motion magnitudes are represented in blue in Fig. 5(a) and (c). The equivalent motion on the detector, $d_x \cos(\theta) + d_y \sin(\theta)$, is shown in blue in Fig. 5(b) and (d).

2) Geometry Offset Simulation: In order to demonstrate the geometry offset calibration ability of our algorithm, we set a $\Delta l = 3$ detector cells (pixels in our case) geometry offset in one

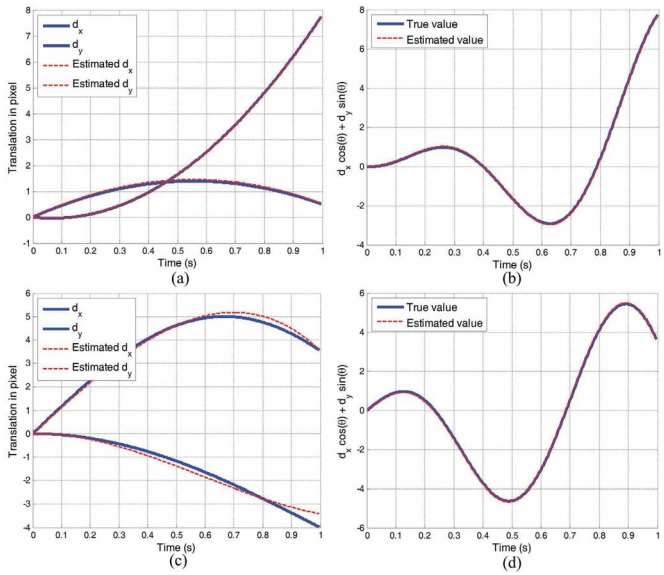

Fig. 5. Translation curves and estimated curves. Images (a) and (b) corresponds to Translation 1 in Table II, and (c) and (d) corresponds to Translation 2.

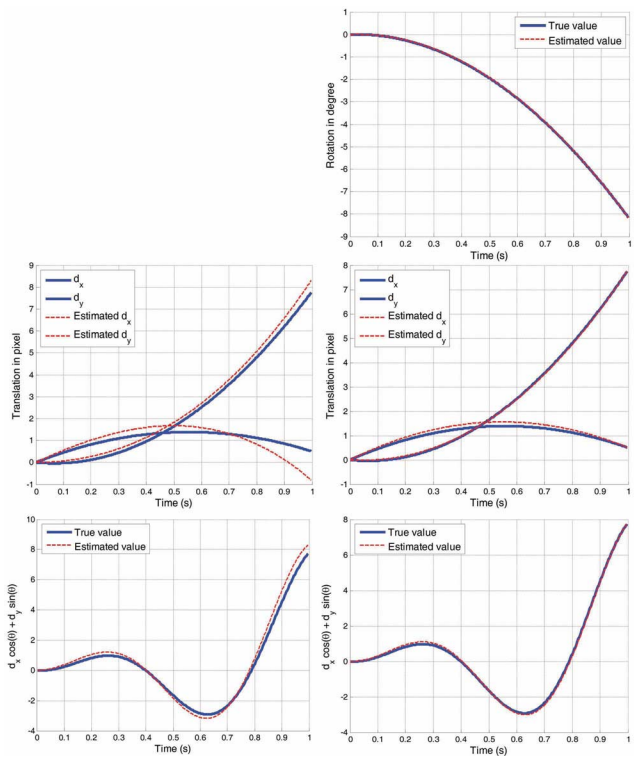

Fig. 6. Estimated curves by translation motion estimation (first column) and general motion estimation (second column).

TABLE III
LIST OF SIMULATION EXPERIMENTS

Experiment	Content
1	Translation 1
2	Translation 2
3	Geometry offset
4	Translation 1 + Geometry offset
5	Translation 1 + Rotation
6	Translation 1 + Rotation + Geometry offset

TABLE IV
QUANTITATIVE EVALUATION OF TRANSLATION ESTIMATION RESULTS

	Experiment 1	Experiment 2
$\hat{d}_x(t)$	$-1.10t + 8.70t^2 + 0.19t^3$	$11.60t - 1.41t^2 - 6.63t^3$
$\hat{d}_y(t)$	$5.29t - 4.83t^2 + 0.07t^3$	$0.57t - 8.73t^2 + 4.72t^3$
MTE	2.77	3.98
rMTE	1.88%	3.95%

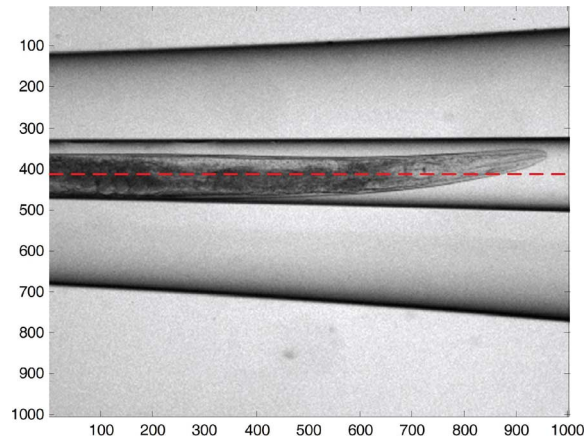

Fig. 7. Projection image of *C. elegans*. The dashed red line denotes the rotation axis position.

of the simulation experiments, which we also combined with translation 1 to verify our algorithm. These two experiments correspond to experiments 3 and 4 in Table III.

3) General Motion Simulation: The rotation function $\phi(t)$ is shown in Table II for which two experiments, termed experiment 5 and 6 in Table III, were simulated. In experiment 5, we combined translation (translation 1) and rotation together. In experiment 6 we combined translation (translation 1), rotation and the $\Delta l = 3$ cells geometry offset together.

B. OPT Imaging

In order to verify the approach with real data, we acquired *in vivo* data from *C. elegans* using a prototype OPT system developed in-house, which has been thoroughly described elsewhere [12], [27], [29]. For the experiment the *C. elegans* was introduced inside a capillary which was placed in a custom-built bath filled with glycerol as an index-matching fluid. A thermoelectrically cooled, electron multiplying CCD with 1002×1004 pixels (Ixon DV885, Andor Technology, Belfast, U.K.) was used to acquire projection images through a $10\times$ objective lens. 500 projections over 360° were acquired in trans-illumination mode. Therefore, $J = 499$ in the *in vivo* experiment. We show one such projection image in Fig. 7.

As was previously mentioned, due to the experimental setup and the fact that the measurements are performed *in vivo*, usually data have significant movement present. The data set we present has been specifically selected since it not only contains movement of the live specimen but also additional geometrical movement of the capillary (note that this movement was not intentional and is due to the capillary not being properly attached to the rotation stage). Hence, this specific data set is perfect to test the translation and general motion calibration algorithm.

Raw data preprocessing was indispensable before motion calibration and image reconstruction in order to apply the FBP algorithm. Assuming $I(\theta)$ represents the projection captured at angle θ, I_0 is the reference image of the system (i.e., constant illumination with no sample), and I_d is the background measurement acquired by the CCD camera when all light sources are switched off, then according to Beer's law, the sum of attenuation coefficients, $g(\theta)$, are

$$g(\theta) = -\log \frac{I(\theta) - I_d}{I_0 - I_d}. \tag{21}$$

The above operation was implemented on the projection image pixel by pixel, and the angular sequence of each row of $g(\theta)$ formed a sinogram, which corresponds to the angular sequence of $g(\theta, l)$ as described in (1). During translation estimation, the parameter T is chosen by minimizing the condition number of the system matrix $\mathbf{M}$, and $T = 1.40$ s in the *in vivo* OPT experiment.

C. Quantitative Evaluation

In order to quantitatively evaluate the motion estimation results, the mean translation excursion (MTE) and the mean rotation excursion (MRE) are defined as follows [38]:

$$\mathrm{MTE} = \int_0^{T_0} \parallel \mathbf{d}(t) \parallel_2 \ \mathrm{d}t/T_0 \tag{22}$$

$$\mathrm{MRE} = \int_0^{T_0} |\phi(t)| \, \mathrm{d}t/T_0 \tag{23}$$

where $\mathbf{d}(t) = (d_x(t), d_y(t))$, and $\parallel (x, y) \parallel_2 = \sqrt{x^2 + y^2}$. T_0 is the total scanning time, and T_0 is set to 1 s in all the simulation experiments. Let $\hat{\mathbf{d}}(t)$ and $\hat{\phi}(t)$ denote the estimated values of the translation and rotation functions, respectively, then the relative mean translation excursion (rMTE) and the relative mean rotation excursion (rMRE) are defined as [38]

$$\mathrm{rMTE} = \frac{\int_0^{T_0} \parallel \hat{\mathbf{d}}(t) - \mathbf{d}(t) \parallel_2 \ \mathrm{d}t}{\int_0^{T_0} \parallel \mathbf{d}(t) \parallel_2 \ \mathrm{d}t}, \tag{24}$$

$$\mathrm{rMRE} = \frac{\int_0^{T_0} |\hat{\phi}(t) - \phi(t)| \, \mathrm{d}t}{\int_0^{T_0} |\phi(t)| \, \mathrm{d}t}. \tag{25}$$

It is clear that the above metrics are just suitable to evaluate the motion estimation results of simulation experiments in which the object motion is known beforehand. In a real experimental situation the object motion is unknown, thus other evaluating indicators should be introduced. Image assessment has been studied by many researchers [41], [42]. Objective metrics of image assessment can be divided into three categories: full-reference, reduced-reference, and no-reference [42]. In the former two cases, full or partial information about the original image should be available. In the last case, the metric is a computed absolute value based on some characteristics of the given image, not relative to a reference image. There is no doubt that a no-reference metric should be adopted in our study.

The assessment of the motion correction results is similar to the autofocusing problem in computer microscopy in which the best image is chosen directly from the acquired images by a computer without any reference images [43], [44]. In [44], Sun *et al.* have tested and compared eighteen widely used focus algorithms and pointed out that the normalized variance method provided the best overall performance. Therefore, the normalized variance is utilized herein to evaluate the motion correction results in our study. The normalized variance is defined as

$$\mathrm{nVar} = \frac{1}{\bar{F} \cdot H \cdot W} \sum_{m=0}^{W-1} \sum_{n=0}^{H-1} (F(m, n) - \bar{F})^2 \tag{26}$$

where F is the reconstructed image of $H \times W$ size, and $\bar{F}$ denotes the mean value of F.

It should be noted that some researchers also use image variance to assess the quality of the reconstructed images [14], [29]. By normalizing the final output with the mean intensity, the normalized variance method can compensate for the differences in average image intensity among different images [44].

IV. Results

A. Simulation Results

Fig. 5 shows the estimated curve through the translation estimation method. The first and second rows correspond to experiments 1 and 2, respectively. In Fig. 8, column 1 and 2 present the reconstructed results without and with translation calibration, respectively. Rows 1 to 4 correspond to experiments 1 to 4 in Table III. The results demonstrate that if there is only translation motion or/and geometry offset, the translation correction method is enough to implement motion calibration. Even though experiment 2 displays some bias of the d_x and d_y estimation, the equivalent motion on detector, $d_x \cos(\theta) + d_y \sin(\theta)$, is found with good accuracy yielding an improved calibrated image.

For the general motion which combines both translation and rotation, performing translation correction on its own is not sufficient, in which case we need to resort to using the general motion correction method. The first and second columns of Fig. 6 show the estimated curve through translation and general motion estimation, respectively. Rows 1 to 3 of Fig. 9 show reconstructed results without correction, with translation correction and with general motion correction, respectively. The first and second columns correspond to the results of experiments 5 and 6, respectively.

Quantitative evaluation of the motion estimation has been done by MTE, MRE, rMTE, and rMRE in this paper. For experiments 3, 4, and 6, there are geometry offsets during simulations, which will be equivalent to a translation motion during motion estimation, and cannot be distinguished from a real translation of the object. Therefore, the motion estimation results cannot be quantitatively evaluated using the above metrics. In the following, only the evaluation results of experiments 1, 2, and 5 will be shown.

The quantitative results of experiments 1 and 2 are listed in Table IV. The rMTE of experiments 1 and 2 are 1.88% and 3.95%, respectively. Polynomial fitting has been used to approximate the motion translation curve in both experiments 1 and 2. The translation function in experiment 1 is following a polynomial, while in experiment 2 the object is moving along a

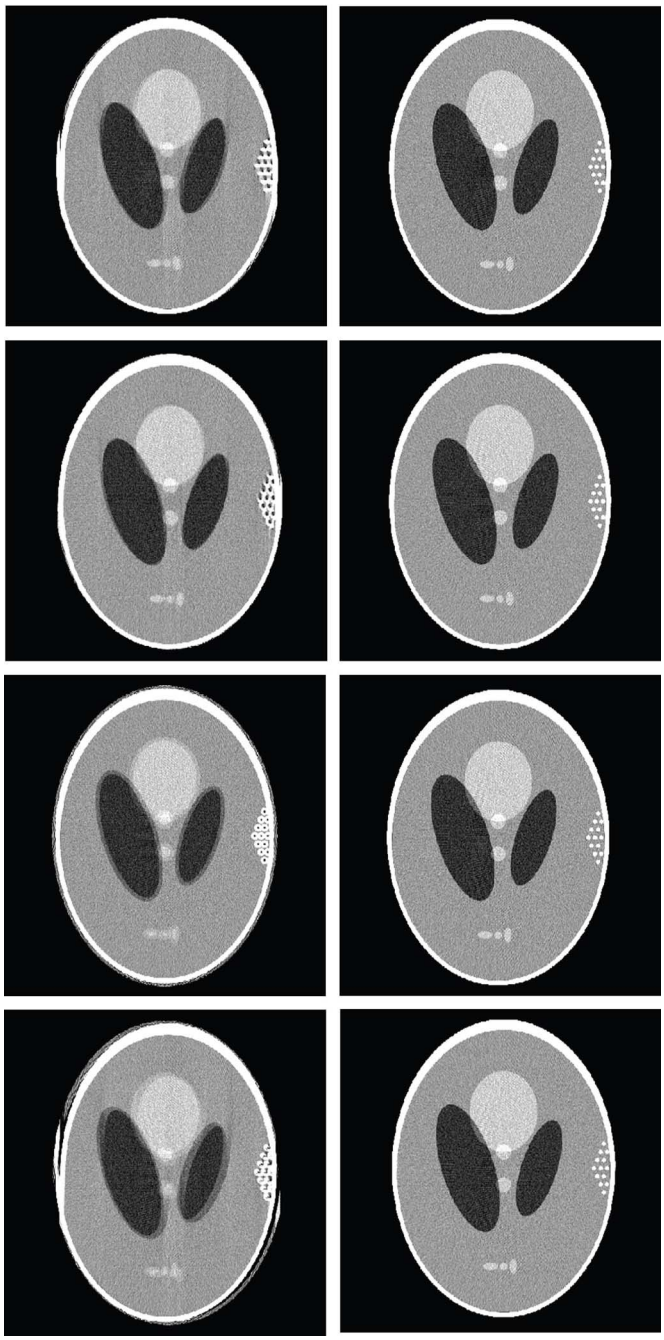

Fig. 8. Reconstructed results without (first column) and with translation correction (second column). Row 1 to 4 corresponds to experiments 1 to 4 in Table III. The display window is $[0.9, 1.1]$.

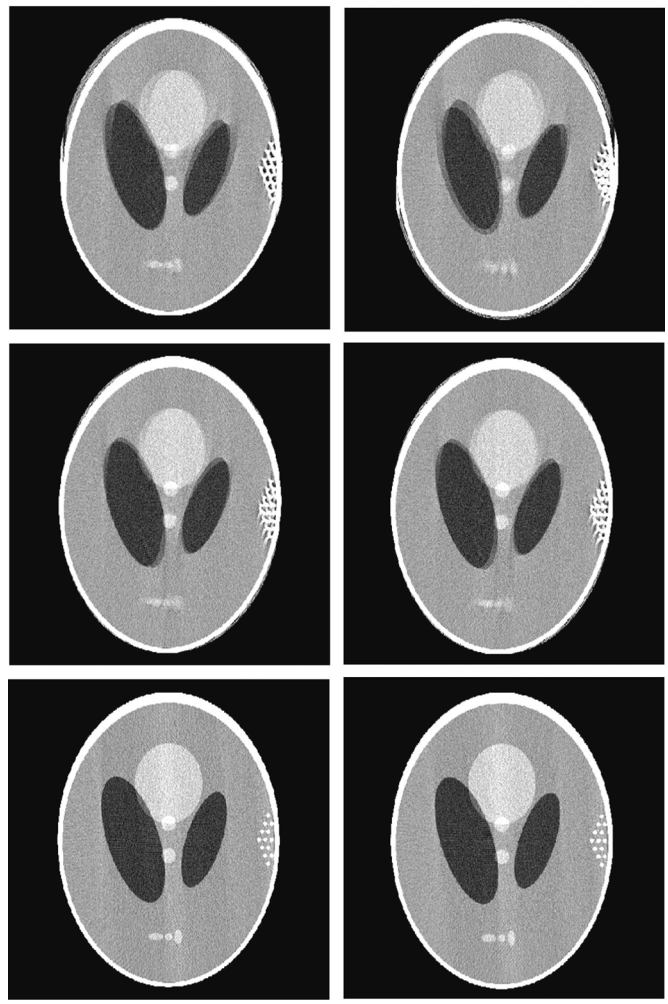

Fig. 9. Reconstructed results without correction (first row), with translation correction (second row) and with general motion correction (third row). The first column corresponds to experiment 5, and the second column corresponds to experiment 6 of Table III. The display window is $[0.9, 1.1]$.

TABLE V
QUANTITATIVE EVALUATION OF GENERAL MOTION ESTIMATION RESULTS IN EXPERIMENT 5

	Translation estimation	General motion estimation
$\hat{d}_x(t)$	$0.07t + 6.08t^2 + 2.21t^3$	$11.60t - 1.41t^2 - 6.63t^3$
$\hat{d}_y(t)$	$5.96t - 3.58t^2 - 3.20t^3$	$0.57t - 8.73t^2 + 4.72t^3$
$\hat{\phi}(t)$	-	$0.54t - 8.74t^2$
MTE	2.77	2.77
rMTE	13.73%	4.63%
MRE	-	2.64
rMRE	-	0.88%

sinusoidal curve. As a result, the rMTE in experiment 2 is larger than in experiment 1.

Table V lists the general motion estimation results of experiment 5, which compares the results of the translation estimation method and that of the general motion estimation method. In the general motion case, the rMTE and rMRE of the general motion estimation method are 4.63% and 0.88%, respectively. The rMTE of the translation estimation method is 13.73%, which is obviously larger than the general motion estimation method.

The motion correction results of all the simulation experiments have been evaluated by the normalized variance method. Table VI lists the assessment results of experiments 1 to 4, which shows that the normalized variance value nVar increases significantly after motion correction. Corresponding results for experiments 5 and 6 are shown in Table VII. Both translation and rotation exist in these two experiments. Translation correction can partially increase nVar, and the general motion correction can further improve the correction results. These quantitative evaluation results agree with the results presented in Fig. 9.

TABLE VI
QUANTITATIVE EVALUATION OF TRANSLATION CORRECTION BY NORMALIZED VARIANCE

nVar	Without correction	Translation correction
Experiment 1	0.4924	0.5213
Experiment 2	0.5038	0.5211
Experiment 3	0.4620	0.5211
Experiment 4	0.4618	0.5203

TABLE VII
QUANTITATIVE EVALUATION OF GENERAL MOTION CORRECTION BY NORMALIZED VARIANCE

nVar	Experiment 5	Experiment 6
Without correction	0.4941	0.4656
Translation correction	0.5045	0.5035
General motion correction	0.5464	0.5454

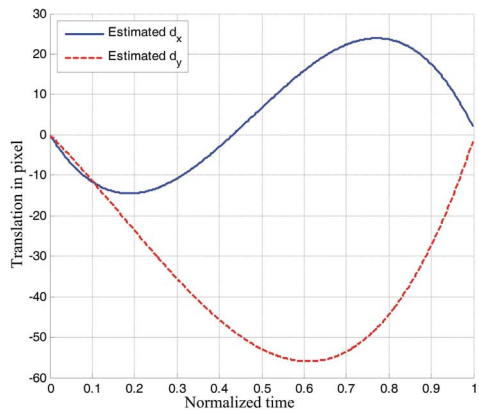

Fig. 10. Estimated translation curve through translation estimation method of *C. elegans* data.

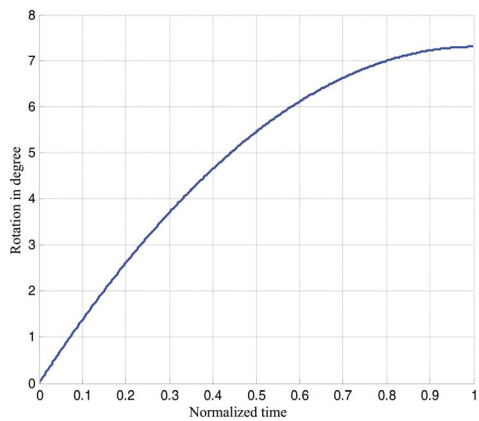

Fig. 11. Estimated rotation curve through general motion estimation method of *C. elegans* data.

B. OPT Imaging Results

Fig. 10 shows the estimated movement curves d_x and d_y of *C. elegans* data through the translation estimation method. Figs. 11 and 12 give the estimated rotation and translation curves through the general motion estimation method. In these three figures the normalized time is adopted to describe the object motion during scanning.

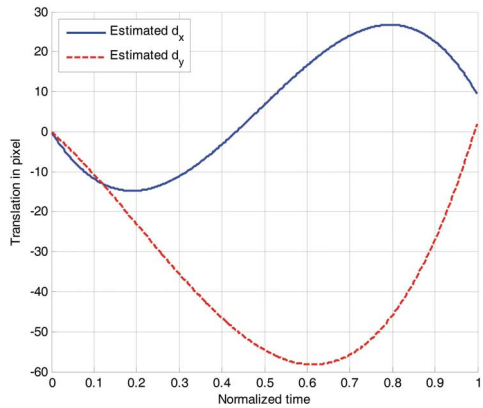

Fig. 12. Estimated translation curve through general motion estimation method of the *C. elegans* data.

Once the movement parameters were obtained, the object could be reconstructed via FBP algorithm with movement compensation. Fig. 13 shows the reconstructed images, where the top two rows correspond to the 720th slice and the 480th slice with positions as indicated by the red and yellow lines in the longitudinal views. Fig. 13(a) corresponds to the reconstructed image without motion calibration. Note that the motion artifacts are easily seen in these views, especially in the transaxial view. Fig. 13(b) depicts the reconstructed results by compensating translation movement shown in Fig. 10. Compared with (a), we can see that the motion artifacts are strongly reduced when using the translation motion correction. Fig. 13(c) shows the reconstructed results calibrated by general motion parameters shown in Figs. 11 and 12. Fig. 13(b) and (c) are very similar, which leads us to conclude that during the OPT imaging session of *C. elegans*, there was significant specimen translation movement which greatly affected the reconstructed results, whereas there was no appreciable rotation of the specimen.

In order to compare the spatial resolution of the reconstructed images, a high contrast region of interest (ROI) has been chosen for analysis. As indicated by the blue rectangles shown in the top two rows of Fig. 13, each thin rectangle represents a 30×10 ROI in the 480th and 720th slices of the reconstructed images respectively. The columns of each ROI were averaged and plotted in Fig. 14. The averaged profiles across the capillary wall of the 720th slices, corresponding to the first row images in Fig. 13, are shown in Fig. 14(a), and Fig. 14(b) corresponds to the 480th slices results. As shown in these figures, the capillary wall was separated into two low peaks before motion correction, and restored to one high peak after motion correction, implying that a significant improvement of spatial resolution was obtained by motion correction. In addition, it can be seen that the results of translation and general motion correction are nearly the same.

A further quantitative evaluation of the motion correction results is given by the normalized variance method. The normalized variance values were calculated for each slice of the reconstructed images without motion correction, the reconstructed images with translation correction and the reconstructed images with general motion correction, respectively. The results are shown in Fig. 15. Fig. 15(a) and (c) shows the mean value and normalized variance of each slice respectively, and Fig. 15(b)

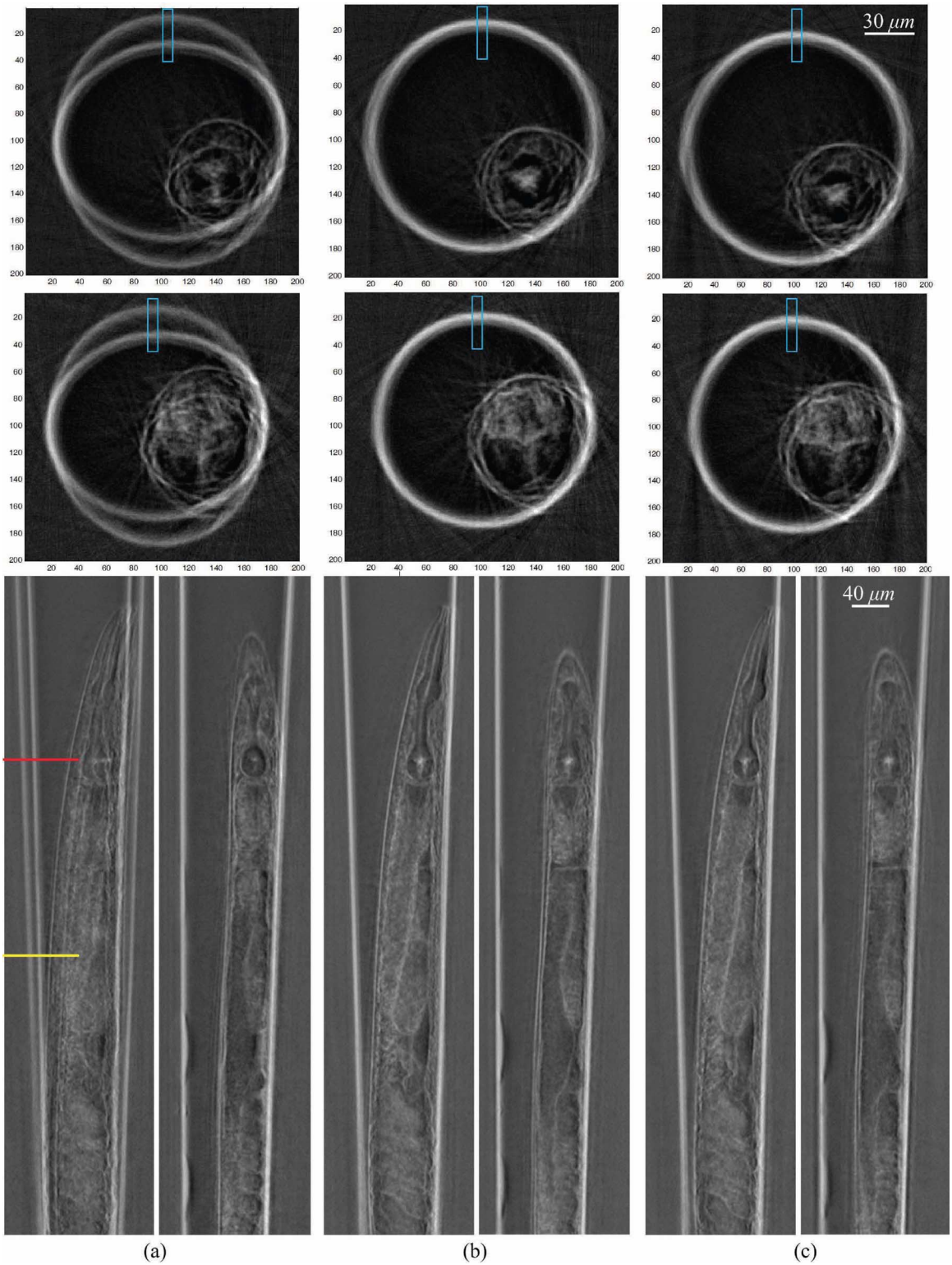

Fig. 13. 3-D reconstruction results from *C. elegans in vivo*. (a) Without motion correction. (b) With translation correction. (c) With general motion correction. The top two rows correspond to the 720th slices and the 480th slices which are indicated by the red and yellow lines in the longitudinal views.

gives a longitudinal view of *C. elegans* to present the corresponding position of each slice. Fig. 15(c) demonstrates that the normalized variance values of the motion correction images, both translation correction and general motion correction, are much higher than the images without motion correction, implying a significant improvement of the image quality after motion correction. Meanwhile, the normalized variance values of translation correction and general motion correction are nearly the same, which can also be seen from the coincidence of the blue and the red lines in Fig. 14. The normalized variance values fluctuate according to the slices, and increase towards the right hand side (anterior part) of specimen due to a decrease of the

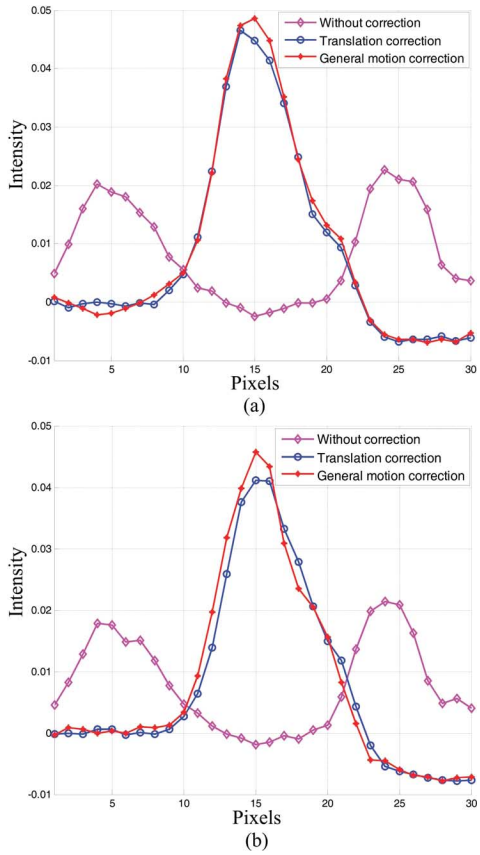

Fig. 14. Averaged profiles across the capillary wall at positions indicated by the blue ROIs shown in Fig. 13. Images (a) and (b) correspond to the first and second row of Fig. 13 respectively.

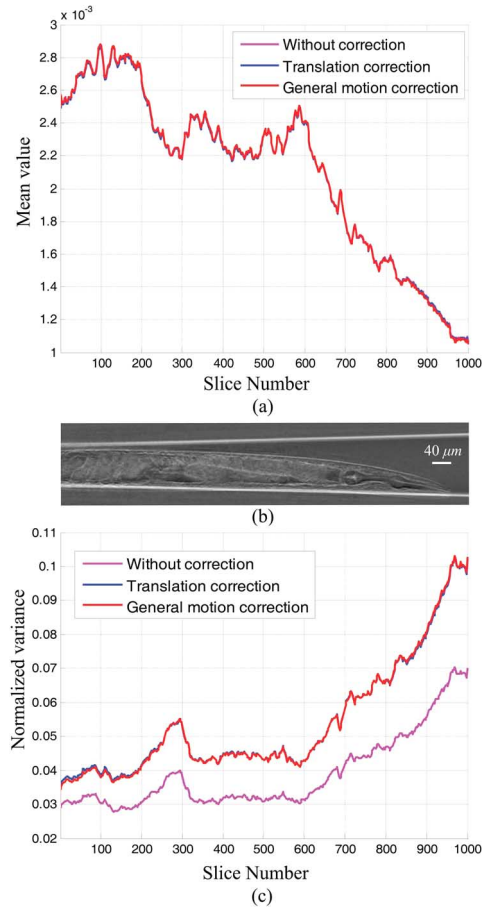

Fig. 15. Quantitative evaluation of the motion correction results by the normalized variance method. (a) Mean value of each slice. (b) Longitudinal view of the *C. elegans*. (c) Normalized variance value of each slice.

diameter of the specimens, i.e., a decrease of the mean value of the slices, as is shown in Fig. 15(b).

It is clear from the above analysis that image resolution is improved significantly after motion correction. Moreover, there is no obvious difference between the translation correction and general motion correction results. The general motion estimation is implemented by a search strategy, which will take a longer time than the translation estimation. In the case of *in vivo* OPT imaging, it seems that the general motion estimation is not warranted since the translation correction has already obtained very good results. However, in the simulation experiments the effect of general motion correction is readily observed. A possible reason can be that the *C. elegans* is very close to the rotation axis during scanning, as is shown in Fig. 7 clearly, in which the dashed red line denotes the rotation axis in OPT imaging. It is well known that the smaller the turning radius, the fewer motion artifacts the rotation makes. In this case, the rotation effect on *C. elegans* imaging, if any, should be very small.

V. Discussion and Conclusion

In this paper we proposed a novel approach for parallel beam OPT motion calibration based on the consistency condition. The approach can estimate the object movement from projection data directly and does not need any other auxiliary information. If the rotation movement is negligible, solving a linear equation is enough to acquire the translation movement information. We have discussed the condition number of the equation and pointed out how to obtain a small condition number during the solution of the equation. If both the rotational and translational movements are present simultaneously, a search strategy is then used to estimate translation and rotation alternatively. In addition, we have shown that the offset of the axis of rotation of the system can be equivalent to object movement and can thus be corrected by our translation estimation method. Therefore, our approach is able to calibrate general motion, including translation and rotation, and the axis of rotation offset of the system *simultaneously*. Due to the relativity of object movement and mechanical movement, our approach is also capable of removing artifacts due to mechanical instability at the same time.

A numerical evaluation of our algorithm is presented using computer-simulated OPT data. The results demonstrate the efficiency of our approach, which has also been verified using *in vivo* OPT data from *C. elegans*. The *in vivo* results showed a significant decrease in the number of artifacts due to movement when our approach was applied.

Theoretically speaking, there is no size limitation of the geometry offset corrected by our method. However, making motion correction with a very large offset value is not encouraged, since during geometry offset correction the offset value can be equivalently estimated to object translation. Since the translation motion estimated by our method contains two parts, a real object translation and an equivalent translation by the geometry

offset, if the geometry offset is very large compared to the object translation, the proportion of the real object translation in the estimated value will be very small. In this case, a small estimation error will result in a relatively large bias in the real object translation. In fact, a coarse estimation of the geometry offset is very easy. Therefore, we can first estimate the geometry offset coarsely by other methods, using the sinograms for example. Afterwards an accurate estimation of the geometry offset and the object translation can be done *simultaneously* by our method.

In our method, we approximate both translation and rotation through polynomial expressions, in which case the choice of the order of the polynomials N_1 and N_2 is very relevant. A smaller N_1 or N_2 will result in less accurate estimation, while a larger one is also not encouraged since, as is shown in Table I, the higher the value of N_1 the larger the condition number of matrix $\mathbf{M}$, which will result in instability of the translation algorithm. It should be noted that a higher N_1 will not increase computational cost significantly. However, a higher N_2 results in a larger dimension of search space, which will increase the computation demand greatly.

The search time for general motion estimation is related to the search range and to the search step. For example, if using a two-order polynomial expression to fit the rotation, and the search ranges of $p_{3,1}$ and $p_{3,2}$ and are set to $[-10, 10]$ with a search step of 0.1, it takes about 560 ss with an Intel Xeon dual-core CPU W3505@2.53 GHz and 6 GB DDR2 memory. All the search codes have been implemented using Matlab R2010b. A multi-level search strategy can be used to reduce the computation time, which means a coarse search with a large range and large step is performed first to find a preliminary value of $p_{3,1}$ and $p_{3,2}$, then a refined search around the preliminary value with small step is adopted for an accurate estimation.

One point which needs attention is that a very large number of projections will not increase the search time significantly. This is due to the object motion being estimated by polynomial fitting, which just needs to obtain the finite order polynomial coefficients and does not need to consider each separate projection. More projection images mean more data can be used for polynomial fitting, but will not lead to a dramatic computation increase. Therefore, our method can be utilized to deal with large time-lapse scan sets without added complexity.

Because our method utilizes the symmetry for rotation estimation as shown in (20), a full 360° scanning is recommended. When the scanning range is between 180° and 360°, in which case only a few projection data satisfy symmetry, the rotation estimation method could cease to be effective. For full 360° measurements, the actual rotation range will be less than or more than 360° due to specimen rotational movement. Assuming the rotation of the specimen is less than 30°, this will not affect the rotation estimation method since there will still be enough projections to satisfy symmetry.

In this paper, our attention was focused on parallel beam OPT only. For fan beam or cone beam OPT motion estimation, we suggest the work on fan beam X-ray CT motion calibration [37], [38]. It should be noted that there are some limitations to our approach: firstly, projection truncation is not allowable, a restriction which results from the consistency condition. Secondly, our approach is currently valid for trans-illumination OPT imaging, and is not suitable for fluorescence imaging. This is because in fluorescence mode there is no reference image as is in trans-illumination mode, since the fluorescence from a certain section might be visible from one side of the specimen and barely visible from the opposite side due to different absorption and/or scattering properties. Added to this is the fact that the movement of the specimen in and out of the focal plane while measuring all OPT projections has a very strong effect on our motion calibration method. Note, however, that this issue can be corrected for by increasing the depth of field of the objective. What we suggest is to measure simultaneously, or at least sequentially, excitation and emission data in order to accurately and automatically account for specimen movement both in fluorescence and trans-illumination OPT since in this case it would be safe to assume that specimen movement is equivalent in both modes. The limitations that the motion calibration presents in fluorescence data might also be overcome by introducing the attenuation compensation in fluorescence OPT as done in [4], [45], and thus account for the heterogeneity of the sample. We believe that our motion calibration method combined with the attenuation compensation of fluorescence OPT data will significantly improve resolution, quantitation and quality in general of *in vivo* OPT data. Thirdly, in this paper just the object motion in-plane was studied, neglecting the longitudinal motion. In order to estimate the longitudinal motion, there are two feasible strategies. The first strategy is suitable for the case where there are some high contrast points on the object which can be used as tracking markers, and the longitudinal motion information can be extracted from these markers in multiple projection images [29]. The second strategy is a more general method, which is suitable for the case where high contrast structured object features are missing and have to estimate the z-direction motion from common projections. For example, Pauchard *et al.* proposed a method to determine longitudinal translations by tracking profiles of the object among projections [46]. Combining such strategies with our in-plane motion estimation method, the 3-D motion of OPT imaging can be corrected, which is the focus of future studies.

Appendix A
Derivation of the Consistency Condition

Substituting (1) into (3), we then have

$$\begin{aligned} v_k(\theta) &= \int_{-\infty}^{+\infty} l^k \iint_C f(x,y)\delta(x\cos\theta + y\sin\theta - l)\,\mathrm{d}x\,\mathrm{d}y\,\mathrm{d}l \\ &= \iint_C f(x,y)\int_{-\infty}^{+\infty} l^k \delta(x\cos\theta + y\sin\theta - l)\,\mathrm{d}l\,\mathrm{d}x\,\mathrm{d}y \\ &= \iint_C f(x,y)(x\cos\theta + y\sin\theta)^k\,\mathrm{d}x\,\mathrm{d}y \\ &= \iint_C \sum_{r=0}^{k}\binom{k}{r}(x\cos\theta)^r(y\sin\theta)^{k-r} f(x,y)\,\mathrm{d}x\,\mathrm{d}y \\ &= \sum_{r=0}^{k}\binom{k}{r}\cos^r\theta\sin^{k-r}\theta\iint_C x^r y^{k-r} f(x,y)\,\mathrm{d}x\,\mathrm{d}y \end{aligned} \tag{A1}$$

where $\binom{k}{r} = (k!)/(r!(k-r)!)$. Substituting (2) into the above equation, the HLCC can be expressed as

$$v_k(\theta) = \sum_{r=0}^{k} \frac{k!}{r!(k-r)!} m_{r,k-r} \cos^r\theta \sin^{k-r}\theta. \tag{A2}$$

Appendix B
Effect of the Total Virtual Scanning Time on Motion Correction

In this appendix, we shall prove that replacing the actual total scanning time T_0 with the virtual total scanning time T will not affect the motion estimation results.

For simplification, only a translation of the object in x direction during the OPT experiment is taken into consideration. The proof is the same for the cases of translation in y direction and rotation.

The actual translation along the x axis can be expressed as

$$\tilde{d_x}(s) = \tilde{p}_{1,1}s + \tilde{p}_{1,2}s^2 + \cdots + \tilde{p}_{1,N_1}s^{N_1} \tag{B1}$$

where $0 \le s \le T_0$. During the whole experiment, $J+1$ projections with a uniform scanning interval are acquired. In this case the time to acquire the jth projection is $s_j = j \cdot T_0/J$, where $0 \le j \le J$. For an OPT projection set, if the motion distance $\tilde{d_x}(s_j)$ for each projection is already known, the motion correction can be implemented exactly. The motion distance corresponding to the jth projection can be expressed as

$$\tilde{d_x}(s_j) = \tilde{p}_{1,1}\frac{T_0}{J}j + \tilde{p}_{1,2}\left(\frac{T_0}{J}j\right)^2 + \cdots + \tilde{p}_{1,N_1}\left(\frac{T_0}{J}j\right)^{N_1}. \tag{B2}$$

Assuming that the whole experiment is finished in the virtual total scanning time T, the relationship between T_0 and T is $T = \alpha T_0$, where α is a positive scale coefficient. Correspondingly, $t = \alpha s$, $0 \le t \le T$, and the virtual scanning time to acquire the jth projection is $t_j = j \cdot T/J$.

Substituting s by t/α in (B1), the motion distance for the virtual scanning time t can be expressed as

$$d_x(t) = \frac{\tilde{p}_{1,1}}{\alpha}t + \frac{\tilde{p}_{1,2}}{\alpha^2}t^2 + \cdots + \frac{\tilde{p}_{1,N_1}}{\alpha^{N_1}}t^{N_1}. \tag{B3}$$

Therefore, the motion distance corresponding to the jth projection can be expressed as

$$\begin{aligned} d_x(t_j) &= \frac{\tilde{p}_{1,1}}{\alpha}\frac{T}{J}j + \frac{\tilde{p}_{1,2}}{\alpha^2}\left(\frac{T}{J}j\right)^2 + \cdots \\ &\quad + \frac{\tilde{p}_{1,N_1}}{\alpha^{N_1}}\left(\frac{T}{J}j\right)^{N_1} \\ &= \frac{\tilde{p}_{1,1}}{\alpha}\frac{\alpha T_0}{J}j + \frac{\tilde{p}_{1,2}}{\alpha^2}\left(\frac{\alpha T_0}{J}j\right)^2 + \cdots \\ &\quad + \frac{\tilde{p}_{1,N_1}}{\alpha^{N_1}}\left(\frac{\alpha T_0}{J}j\right)^{N_1} \\ &= \tilde{p}_{1,1}\frac{T_0}{J}j + \tilde{p}_{1,2}\left(\frac{T_0}{J}j\right)^2 + \cdots \\ &\quad + \tilde{p}_{1,N_1}\left(\frac{T_0}{J}j\right)^{N_1}. \end{aligned} \tag{B4}$$

Comparing (B2) and (B4), it can be clearly seen that $\tilde{d_x}(s_j) = d_x(t_j)$, which means the choice of T will not affect the description of the motion distance for a certain projection, and therefore replacing T_0 with T will not affect the motion correction results.

Let $p_{1,k} = \tilde{p}_{1,k}/\alpha^k$ in (B3), where $1 \le k \le N_1$, then

$$d_x(t) = p_{1,1}t + p_{1,2}t^2 + \cdots + p_{1,N_1}t^{N_1}. \tag{B5}$$

This has the same form as in (11).

Acknowledgment

The authors would like to thank anonymous reviewers for their valuable comments that made possible a substantial improvement of the first version of this paper.

References

[1] J. Sharpe, U. Ahlgren, P. Perry, B. Hill, A. Ross, J. Hecksher-Sorensen, R. Baldock, and D. Davidson, "Optical projection tomography as a tool for 3-D microscopy and gene expression studies," *Science*, vol. 296, pp. 541–545, 2002.

[2] J. Sharpe, "Optical projection tomography as a new tool for studying embryo anatomy," *J. Anatomy*, vol. 202, pp. 175–181, 2003.

[3] J. Sharpe, "Optical projection tomography," *Annu. Rev. Biomed. Eng.*, vol. 6, pp. 209–228, 2004.

[4] A. Thomas, J. Bowsher, J. Roper, T. Oliver, M. Dewhirst, and M. Oldham, "A comprehensive method for optical-emission computed tomography," *Phys. Med. Biol.*, vol. 55, pp. 3947–3957, 2010.

[5] A. Papadakis, G. Zacharakis, T. Maris, J. Ripoll, and J. Damilakis, "A new optical-CT apparatus for three-dimensional radiotherapy dosimetry: Is free space scanning feasible?," *IEEE Trans. Med. Imag.*, vol. 29, no. 5, pp. 1204–1212, May 2010.

[6] M. Oldham, H. Sakhalkar, T. Oliver, Y. M. Wang, J. Kirpatrick, Y. Cao, C. Badea, G. A. Johnson, and M. Dewhirst, "Three-dimensional imaging of xenograft tumors using optical computed and emission tomography," *Med. Phys.*, vol. 33, no. 9, pp. 3193–3202, 2006.

[7] M. Oldham, H. Sakhalkar, Y. M. Wang, P. Guo, T. Oliver, R. Bentley, Z. Vujaskovic, and M. Dewhirst, "3-D imaging of whole rodent organs using optical computed and emission tomography," *J. Biomed. Opt.*, vol. 12, p. 014009, 2007.

[8] R. J. Bryson-Richardson and P. D. Currie, "Optical projection tomography for spatio-temporal analysis in the zebrafish," *Method Cell Biol.*, vol. 76, pp. 37–50, 2004.

[9] J. Kerwin, M. Scott, J. Sharpe, L. Puelles, S. C. Robson, M. Martłnez-de-la-Torre, J. L. Ferran, G. Feng, R. Baldock, T. Strachan, D. Davidson, and S. Lindsay, "3 dimensional modelling of early human brain development using optical projection tomography," *BMC Neurosci.*, vol. 5, p. 27, 2004.

[10] M. Fauver, E. J. Seibel, J. R. Rahn, M. G. Meyer, F. W. Patten, T. Neumann, and A. C. Nelson, "Three-dimensional imaging of single isolated cell nuclei using optical projection tomography," *Opt. Exp.*, vol. 13, no. 11, pp. 4210–4223, 2005.

[11] C. Vinegoni, D. Razansky, J.-L. Figueiredo, L. Fexon, M. Pivovarov, M. Nahrendorf, V. Ntziachristos, and R. Weissleder, "Born normalization for fluorescence optical projection tomography for whole heart imaging," *J. Vis. Exp.*, vol. 28, p. 1389, 2009.

[12] M. Rieckher, U. J. Birk, H. Meyer, J. Ripoll, and N. Tavernarakis, "Microscopic optical projection tomography *in vivo*," *PloS ONE*, vol. 6, no. 4, p. e18963, 2011.

[13] A. Darrell, H. Meyer, K. Marias, M. Brady, and J. Ripoll, "Weighted filtered backprojection for quantitative fluorescence optical projection tomography," *Phys. Med. Biol.*, vol. 53, no. 14, pp. 3863–3881, 2008.

[14] J. R. Walls, J. G. Sled, J. Sharpe, and R. M. Henkelman, "Correction of artefacts in optical projection tomography," *Phys. Med. Biol.*, vol. 50, pp. 4645–4665, 2005.

[15] J. R. Walls, J. G. Sled, J. Sharpe, and R. M. Henkelman, "Resolution improvement in emission optical projection tomography," *Phys. Med. Biol.*, vol. 52, pp. 2775–2790, 2007.

[16] Y. Wang and R. K. Wang, "Imaging using parallel integrals in optical projection tomography," *Phys. Med. Biol.*, vol. 51, pp. 6023–6032, 2006.

[17] Y. Wang and R. K. Wang, "Optimization of image-forming optics for transmission optical projection tomography," *Appl. Opt.*, vol. 46, no. 27, pp. 6815–6820, 2007.

[18] J. McGinty, K. B. Tahir, R. Laine, C. B. Talbot, C. Dunsby, M. A. Neil, L. Quintana, J. Swoger, J. Sharpe, and P. M. French, "Fluorescence lifetime optical projection tomography," *J. Biophoton.*, vol. 1, no. 5, pp. 390–394, 2008.

[19] C. Vinegoni, D. Razansky, J.-L. Figueiredo, M. Nahrendorf, V. Ntziachristos, and R. Weissleder, "Normalized born ratio for fluorescence optical projection tomography," *Opt. Lett.*, vol. 34, no. 3, pp. 319–321, 2009.

[20] F. Vasefi, E. Ng, B. Kaminska, G. H. Chapman, K. Jordan, and J. J. L. Carson, "Transmission and fluorescence angular domain optical projection tomography of turbid media," *Appl. Opt.*, vol. 48, no. 33, pp. 6448–6457, 2009.

[21] C. Vinegoni, L. Fexon, P. F. Feruglio, M. Pivovarov, J. L. Figueiredo, M. Nahrendorf, A. Pozzo, A. Sbarbati, and R. Weissleder, "High throughput transmission optical projection tomography using low cost graphics processing unit," *Opt. Exp.*, vol. 17, no. 25, pp. 22320–22332, 2009.

[22] P. F. Feruglio, C. Vinegoni, J. Gros, A. Sbarbati, and R. Weissleder, "Block matching 3-D random noise filtering for absorption optical projection tomography," *Phys. Med. Biol.*, vol. 55, pp. 5401–5415, 2010.

[23] R.-A. Lorbeer, M. Heidrich, C. Lorbeer, D. Fernando, R. Ojeda, G. Bicker, H. Meyer, and A. Heisterkamp, "Highly efficient 3-D fluorescence microscopy with a scanning laser optical tomograph," *Opt. Exp.*, vol. 19, no. 6, 2011.

[24] M. J. Boot, C. H. Westerberg, J. Sanz-Ezquerro, J. Cotterell, R. Schweitzer, M. Torres, and J. Sharpe, "*In vitro* whole-organ imaging: 4D quantification of growing mouse limb buds," *Nat. Methods*, vol. 5, pp. 609–612, 2008.

[25] J. F. Colas and J. Sharpe, "Live optical projection tomography," *Organogenesis*, vol. 5, no. 4, pp. 211–216, 2009.

[26] A. Cheddad, C. Svensson, J. Sharpe, F. Georgsson, and U. Ahlgren, "Image processing assisted algorithms for optical projection tomography," *IEEE Trans. Med. Imag.*, vol. 31, no. 1, pp. 1–15, Jan. 2012.

[27] H. Meyer, A. Darrell, A. Metaxakis, C. Savakis, and J. Ripoll, "Optical projection tomography for *in-vivo* imaging of drosophila melanogaster," *Microscopy Anal.*, vol. 22, pp. 1–6, 2008.

[28] J. Ripoll, H. Meyer, and A. Garofalakis, "*In vivo* optical tomography: From diffusion to ballistic," *Opt. Mater.*, vol. 31, pp. 1082–1085, 2009.

[29] U. J. Birk, M. Rieckher, N. Konstantinides, A. Darrell, A. Sarasa-Renedo, H. Meyer, N. Tavernarakis, and J. Ripoll, "Correction for specimen movement and rotation errors for *in-vivo* optical projection tomography," *Biomed. Opt. Exp.*, vol. 1, no. 1, pp. 87–96, 2010.

[30] C. J. Ritchie, C. R. Crawford, J. D. Godwin, K. F. King, and Y. Kim, "Correction of computed tomography motion artifacts using pixel-specific backprojection," *IEEE Trans. Med. Imag.*, vol. 15, no. 3, pp. 333–342, Jun. 1996.

[31] N. C. Linney and P. H. Gregson, "Organ motion detection in CT images using opposite rays in fan-beam projection systems," *IEEE Trans. Med. Imag.*, vol. 20, no. 11, pp. 1109–1122, Nov. 2001.

[32] W. G. Lu and T. R. Mackie, "Tomographic motion detection and correction directly in sinogram space," *Phys. Med. Biol.*, vol. 47, no. 8, pp. 1267–1284, 2002.

[33] X. Jin, L. Li, Z. Chen, L. Zhang, and Y. Xing, "Motion-compensated reconstruction method based on rigid motion model with multi-object," *Tsinghua Sci. Technol.*, vol. 15, no. 1, pp. 120–126, 2010.

[34] F. Natterer, *The Mathematics of Computerized Tomography*. New York: Wiley, 1986.

[35] S. Basu and Y. Bresler, "Uniqueness of tomography with unknown view angles," *IEEE Trans. Image Process.*, vol. 9, no. 6, pp. 1094–1106, Jun. 2000.

[36] H. Y. Yu, X. Q. Mou, and Y. L. Cai, "Calibration of cone beam rotational X-ray image sequence," *Chinese J. Electron.*, vol. 13, no. 3, pp. 424–428, 2004.

[37] H. Y. Yu, Y. C. Wei, J. Hsieh, and G. Wang, "Data consistency based translational motion artifact reduction in fan-beam CT," *IEEE Trans. Med. Imag.*, vol. 25, no. 6, pp. 792–803, Jun. 2006.

[38] H. Y. Yu and G. Wang, "Data consistency based rigid motion artifact reduction in fan-beam CT," *IEEE Trans. Med. Imag.*, vol. 26, no. 2, pp. 249–260, Feb. 2007.

[39] Y.-W. Leung and Y. Wang, "An orthogonal genetic algorithm with quantization for global numerical optimization," *IEEE Trans. Evol. Comput.*, vol. 5, no. 1, pp. 41–53, Feb. 2001.

[40] J. Hsien, *Computed Tomography Principles, Design, Artifacts*. Bellingham, WA: SPIE Press, 2003.

[41] Z. Wang, A. C. Bovik, H. R. Sheikh, and E. P. Simoncelli, "Image quality assessment: From error visibility to structural similarity," *IEEE Trans. Image Process.*, vol. 13, no. 4, pp. 600–612, Apr. 2004.

[42] R. Ferzli and L. J. Karam, "A no-reference objective image sharpness metric based on the notion of just noticeable blur (JNB)," *IEEE Trans. Image Process.*, vol. 18, no. 4, pp. 717–728, Apr. 2009.

[43] F. C. A. Groen, I. T. Young, and G. Ligthart, "A comparison of different focus functions for use in autofocus algorithms," *Cytometry*, vol. 12, pp. 81–91, 1985.

[44] Y. Sun, S. Duthaler, and B. J. Nelson, "Autofocusing in computer microscopy: Selecting the optimal focus algorithm," *Microsc. Res. Techn.*, vol. 65, pp. 139–149, 2004.

[45] C. Vinegoni, C. Pitsouli, D. Razansky, N. Perrimon, and V. Ntziachristos, "*In vivo* imaging of drosophila melanogaster pupae with mesoscopic fluorescence tomography," *Nat. Methods*, vol. 5, no. 1, pp. 45–47, 2008.

[46] Y. Pauchard, F. J. Ayres, and S. K. Boyd, "Automated quantification of three-dimensional subject motion to monitor image quality in high-resolution peripheral quantitative computed tomography," *Phys. Med. Biol.*, vol. 56, pp. 6523–6543, 2011.